PHYSICS

Trapped-ion quantum simulation of electron transfer models with tunable dissipation

Visal So[1]†, Midhuna Duraisamy Suganthi[1,2]†, Abhishek Menon[1], Mingjian Zhu[1], Roman Zhuravel[1], Han Pu[1], Peter G. Wolynes[1,3,4,5], José N. Onuchic[1,3,4,5], Guido Pagano[1]*

Electron transfer is at the heart of many fundamental physical, chemical, and biochemical processes essential for life. The exact simulation of these reactions is often hindered by the large number of degrees of freedom and by the essential role of quantum effects. Here, we experimentally simulate a paradigmatic model of molecular electron transfer using a multispecies trapped-ion crystal, where the donor-acceptor gap, the electronic and vibronic couplings, and the bath relaxation dynamics can all be controlled independently. By manipulating both the ground-state and optical qubits, we observe the real-time dynamics of the spin excitation, measuring the transfer rate in several regimes of adiabaticity and relaxation dynamics. Our results provide a testing ground for increasingly rich models of molecular excitation transfer processes that are relevant for molecular electronics and light-harvesting systems.

INTRODUCTION

Quantum devices hold the promise to provide an advantage in directly simulating many-body quantum systems (1). Chemical reaction dynamics provides a wide range of target applications. Fully realistic digitization of the real-time dynamics of molecules on fault-tolerant quantum computers, however, requires qubit numbers and circuit depths that exceed the current state of the art (2). A promising alternative approach is to develop programmable analog quantum simulators (3–5) that map the dynamical degrees of freedom of molecules directly onto the quantum hardware, therefore providing a more direct but problem-specific quantum advantage.

One outstanding challenge is modeling the real-time electron transfer (ET) dynamics in molecular systems embedded in biological environments. In these systems, the energy differences between the electronic states, molecular vibrational energies, and their mutual couplings are all of the same order of magnitude. This requires simulating electronic excitations while taking into account a large number of nuclear degrees of freedom. In addition, reactions at low temperatures in many molecular systems, ranging from myoglobin ligand recombination (6) to charge transport in DNA strands (7), suggest that quantum effects play a key role.

In many regimes, the reaction dynamics can be treated using imaginary-time path-integral methods (8–10). It has also proven expedient to treat the nuclear and electronic degrees of freedom using a mix of quantum and classical dynamics (11), but the limits of this approach are not always clear. When quantum coherences between the electronic and vibrational degrees of freedom (12, 13) are relevant, such approaches are only approximate. Methods based on the hierarchical equations of motion approach (14), tensor networks (15–17), and real-time path-integral evaluations (18, 19) have also made progress in those regimes.

Recently, the high degree of control and tunability of programmable quantum platforms such as trapped ions, superconducting qubits, and photonic simulators have been used to experimentally simulate models of vibrationally assisted energy transfer (20), conical intersections (21–23), noise-assisted excitation transfer (24, 25), ET driven by polarized light (26), and molecular vibrational dynamics (27).

In this work, we show that a trapped-ion quantum simulator with independent control of unitary and dissipative processes can successfully simulate a paradigmatic ET model. This is achieved by manipulating two different atomic ion species and using both ground-state and optical qubits, combining spin and spin-motion coherent manipulation with sympathetic cooling (28, 29) of a collective bosonic mode. This programmable open quantum system enables the measurement of the time-resolved dynamics of the system in contact with an engineered bosonic bath, accessing nonperturbative regimes, where electronic and vibrational excitations, their mutual coupling, and the relaxation rate are all of the same order of magnitude.

RESULTS

An effective model that describes ET is the celebrated spin-boson model (30). Here, the electronic degrees of freedom are mapped onto a two-level system coupled to a bath of harmonic vibrations encoded in a collection of bosonic modes. This model involves one two-level system, encoding the electron donor and acceptor states, and a reaction coordinate encoded in a single bosonic mode, which is, in turn, itself coupled to a continuous bath of harmonic oscillators (31, 32). Despite its simplicity, this model allows experimental access to paradigmatic ET regimes by measuring the real-time dynamics of the two-level system and extracting the transfer rate as a function of its coupling to the bosonic mode, the electronic donor-acceptor coupling, their energy difference, and the relaxation rate. The central system is described by the following Hamiltonian (31, 33, 34), which is a variant of the Rabi model (35) in quantum optics ($\hbar = 1$)

$$H_s = \frac{\Delta E}{2}\sigma_z + V_x\sigma_x + \frac{g}{2}\sigma_z\left(a^\dagger + a\right) + \omega a^\dagger a \qquad (1)$$

[1]Department of Physics and Astronomy, Rice University, Houston, TX 77005, USA. [2]Applied Physics Graduate Program, Smalley-Curl Institute, Rice University, Houston, TX 77005, USA. [3]Department of Chemistry, Rice University, Houston, TX 77005, USA. [4]Center for Theoretical Biological Physics, Rice University, Houston, TX 77005, USA. [5]Department of Biosciences, Rice University, Houston, TX 77005, USA.
*Corresponding author. Email: pagano@rice.edu
†These authors contributed equally to this work.

where $\sigma_{x,z}$ are the Pauli matrices and $a^{\dagger}(a)$ is the creation (annihilation) operator of the bosonic mode at frequency ω. The reaction coordinate is expressed in terms of the position operator as $y = y_0(a^{\dagger} + a)/2$, with $y_0 = \sqrt{1/2m\omega}$ and m being the particle mass. In this model, when $V_x = 0$, the energy spectrum is described by two harmonic wells assigned to the donor and acceptor states, $|D\rangle \equiv |\uparrow\rangle_z$ and $|A\rangle \equiv |\downarrow\rangle_z$, separated by a relative energy shift ΔE (aka exothermicity). The electronic coupling V_x mixes the states associated with the donor and acceptor surfaces. The spin-boson coupling g displaces the two coupled surfaces along the reaction coordinate, as shown in Fig. 1B. In ET, this is akin to the nuclear coupling that gives rise to the activation energy of a typical ET reaction, which is the core of the Marcus theory (36) in chemistry and polaron theory in solid state physics (37).

Crucially, the full ET Hamiltonian $H_{ET} = H_s + H_b + H_{sb}$ must also include bath degrees of freedom H_b, generally modeled as a large collection of harmonic oscillators, and a linear coupling H_{sb} between the bath and the system's bosonic degree of freedom (31). The bath correlation functions and their effect on the system can be described by a continuous spectral density function $J(\omega)$. One way to create an analog for the structured bath spectral densities of biological environments using trapped ions is to use multiple phononic modes naturally hosted in an ion crystal (38, 39). Here, we take a different approach by exploiting the fact that, under certain conditions, a harmonic environment with a continuous spectral density can be obtained by cooling a spectator ion (40). In section S6, we prove that sympathetic cooling can effectively simulate an ohmic spectral density $J(\omega) \sim \omega$, a common choice in the ET literature. The cooling process can be described by a master equation in terms of Lindbladian superoperators $\mathcal{L}_c[\rho]$, where c is a generic jump operator

$$\frac{\partial \rho}{\partial t} = -i[H_s, \rho] + \gamma(\bar{n}+1)\mathcal{L}_a[\rho] + \gamma\bar{n}\mathcal{L}_{a^{\dagger}}[\rho] \quad (2)$$

$$\mathcal{L}_c[\rho] = c\rho c^{\dagger} - \frac{1}{2}\{c^{\dagger}c, \rho\} \quad (3)$$

Here, ρ is the density matrix of the spin-boson system, γ is the motional relaxation rate, and $\bar{n}$ is the phonon population determined by the temperature of the bath $k_B T = \omega/\log(1+1/\bar{n})$.

The dynamics of the spin and the bosonic observables predicted by Eq. 2 are essentially indistinguishable from those of the system in Eq. 1 in contact with an ohmic bath, provided that the damping is weak ($\gamma \ll \omega$) and the bath thermal energy is larger than the relaxation rate ($\gamma\beta \ll 1$, with $\beta = 1/k_B T$) (40). As shown in the following, these conditions can be realized experimentally with a trapped-ion system, where the dynamics is determined by five parameters $(\omega, \Delta E, V_x, g, \text{and } \gamma)$ that can all be tuned independently. Notably, all the timescales associated with these parameters are faster than the spin and motional decoherence associated with experimental imperfections (see dashed and solid lines in Fig. 1C and section S3), allowing the full characterization of both the transient dynamics and the steady state of the system under Eq. 2.

The experimental setup consists of one $^{171}\text{Yb}^+$ ion and one $^{172}\text{Yb}^+$ ion confined in a linear Paul trap. The two-level system is encoded in the two hyperfine clock states of the $^{171}\text{Yb}^+$ ground-state qubit, $|^2S_{1/2}, F=1, m_F=0\rangle \equiv |\uparrow\rangle_z$ and $|^2S_{1/2}, F=0, m_F=0\rangle \equiv |\downarrow\rangle_z$, separated by a frequency of $\omega_{hf}/2\pi = 12.642$ GHz (see Fig. 1A). The bosonic mode in Eq. 1 is encoded in the radial tilt collective mode at frequency $\omega_{tilt}/2\pi = 3.207$ MHz (see Materials and Methods).

We engineer H_s in Eq. 1 in a driven rotating frame: Two $\pi/2$ pulses are used to map the z spin basis of Eq. 1 onto the y basis. In this configuration, two laser tones resonant with the qubit frequency realize the ΔE and V_x terms. Two additional laser tones at frequencies $\pm\mu = \pm(\omega_{tilt}+\delta)$ from the qubit resonance realize the spin-phonon coupling and the harmonic terms in Eq. 1, where $\delta \equiv -\omega$ is the detuning with respect to the tilt mode (41). All the terms in H_s are engineered using a 355-nm pulsed laser addressing the $^{171}\text{Yb}^+$ ground-state qubit via stimulated Raman transitions (see Fig. 1A and section S1).

Simulating an independently tunable bath dissipation is achieved by driving the narrow transition from the ground state $|g\rangle \equiv |^2S_{1/2}\rangle$ to the optical metastable state $|o\rangle \equiv |^2D_{3/2}\rangle$ of a $^{172}\text{Yb}^+$ ion. Two tones of a 435-nm laser combined with a 935-nm repumper are used
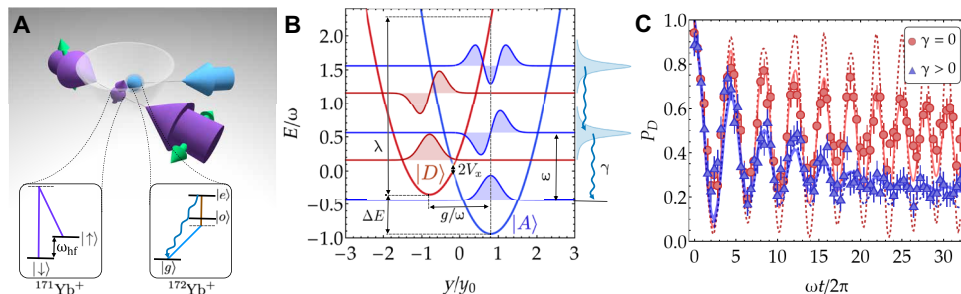

Fig. 1. Simulating ET model with tunable dissipation. (**A**) $^{171}\text{Yb}^+$-$^{172}\text{Yb}^+$ ion crystal confined in a harmonic potential with Coulomb interactions defining normal modes of motion. The ground-state qubit of $^{171}\text{Yb}^+$ encodes the spin degree of freedom and is coherently manipulated by two counterpropagating 355-nm Raman beams (purple arrows, with green arrows showing the light polarization). The optical qubit of $^{172}\text{Yb}^+$ is addressed with a 435-nm laser (blue arrow) and, together with a 935-nm repumper (brown line in the inset), is used for sympathetic cooling. Insets: simplified level schemes for $^{171}\text{Yb}^+$ and $^{172}\text{Yb}^+$. (**B**) Donor (red) and acceptor (blue) surfaces defined by Eq. 1 with parameters $(V_x, g, \Delta E) = (0.06, 1.6, 0.6)\omega$ shown as a function of the reaction coordinate y with their respective noninteracting harmonic wave functions. The bath is represented by vibrational modes with a finite linewidth γ. The color hue reflects the weights of the spin population at each position y. (**C**) Donor population dynamics governed by unitary (red circles) and dissipative (blue triangles) processes with $(V_x, g, \Delta E) = (0.18, 1, 1)\omega$ compared to the numerical results: The dashed lines with $\gamma = 0$ (red) and $\gamma = 0.014\omega$ (blue) are calculated from Eq. 2, whereas their corresponding solid lines also include spin decoherence ($\gamma_z = 0.0013\omega$) and motional dephasing ($\gamma_m = 0.0013\omega$) (see section S3). Error bars are the statistical SEM.

to perform sympathetic cooling (*42*) on the tilt mode with a cooling rate $\gamma / 2\pi$, which is tunable over the 50- to 500-Hz range (see Fig. 1A). This setting is well suited to achieve efficient sympathetic cooling because the fractional mass imbalance of the two ions is very small, and the $|g\rangle \rightarrow |o\rangle$ transition linewidth allows for large Rabi frequencies at modest laser power while providing negligible crosstalk with the qubit states of $^{171}\mathrm{Yb}^+$.

The experimental protocol (see Fig. 2) consists of the following steps: (i) After Doppler cooling, Raman-resolved sideband cooling is applied to both the radial center-of-mass and tilt modes. The resulting initial tilt mode phonon population is in the $\overline{n}_0 \sim (0.1\ \text{to}\ 0.3)$ range, which is comparable to $\overline{n}$ defined in Eq. 2 and characterized independently by measuring the phonon steady state of the purely dissipative evolution without coherent driving (see fig. S1D). (ii) Then, by applying a $\pi / 2$ pulse followed by a displacement operator $\mathcal{D}(-g/2\omega)$, we initialize the system in the donor vibronic state $|D\rangle\langle D| \otimes \rho_-$, where $\rho_- = \sum_n e^{-n\omega/k_B T} |n_-\rangle\langle n_-|$ is a thermal state with temperature $k_B T \approx \omega / \log(1 + 1/\overline{n})$ and $|n_\pm\rangle = \mathcal{D}(\pm g/2\omega)|n\rangle$ are displaced Fock states. (iii) We simultaneously apply the laser tones to generate the ET dynamics described by Eq. 2. All the parameters that determine the unitary and the dissipative evolutions are calibrated independently (see section S2). (iv) At the end of the evolution, after a final $\pi / 2$ pulse, we use state-dependent fluorescence to measure the probability of the system being in the donor state $P_D = (\langle\sigma_z\rangle + 1)/2$ or the average phonon population $\langle n\rangle$ of the tilt mode.

The average number of phonons $\overline{n}$ in the (0.1 to 0.3) range fulfills the condition $k_B T \lesssim \omega$ while making sure that the constraint $\gamma \ll k_B T$ is also satisfied. In this highly quantum regime, the transfer is dominated by the discrete level structure of the vibrational mode, and the temperature has a limited effect on the transfer rate. This corresponds to the low-temperature, tunneling-dominated regime of ET.

A crucial parameter for the ET dynamics is the Marcus reorganization energy $\lambda = g^2/\omega$, which is the amount of energy required to displace a wave packet by g/ω from the center of the donor surface without transferring to the acceptor surface (see Fig. 1B). The

reorganization energy, in turn, determines the classical activation energy $U = (\Delta E + \lambda)^2 / 4\lambda$, which is the barrier a wave packet localized in the donor surface would have to overcome to enter the acceptor surface when the electronic coupling V_x is negligible.

We individuate and investigate two regimes (*33*): a nonadiabatic and a strongly adiabatic transfer regime. In the former, the electronic coupling V_x is a small perturbation with respect to the other energy scales in the Hamiltonian in Eq. 1 and is comparable or smaller than the relaxation rate $(V_x \lesssim \gamma)$. When V_x is also much less than $\lambda/4$, namely, the activation energy at $\Delta E = 0$, the bosonic wave packet is largely localized on either the donor or the acceptor surface, and the ET can be described by the Fermi golden rule (FGR) leading to characteristic isolated peaks in the transfer rate spectrum. Conversely, in the strongly adiabatic regime, the electronic coupling becomes comparable with the activation energy $(V_x \sim \lambda/4)$ and greater than the relaxation rate $(V_x > \gamma)$, changing the shapes of the donor and acceptor surfaces. In this regime, the transfer rate is less sensitive to the electronic coupling V_x and cannot be predicted by the FGR. Increasing V_x lowers the barrier, and the eigenmodes of Hamiltonian in Eq. 1 become closer to delocalized wave packets on the two nonadiabatic surfaces. In this case, one can observe oscillations between the donor and acceptor states before the steady state is reached (see, for example, Fig. 1C). This regime is realized in a type II or type III mixed valence compound (*43*). We note that the adiabatic and nonadiabatic regimes are sometimes also called "coherent" and "incoherent," respectively. However, in this work, we chose the terminology used in chemical kinetics.

Nonadiabatic regime

In the nonadiabatic, low-temperature regime, the transfer is dominated by the vibrational mode structure: Both the unitary and dissipative dynamics are frozen unless the donor-acceptor energy difference nearly matches the vibrational energy at $\Delta E = \ell\,\omega$, with ℓ being an integer greater than zero. This vibrationally assisted dynamics (*20*) results in well-resolved resonances (see Fig. 3). Deep in the nonadiabatic regime, when $|V_x| \ll \lambda/4$, the eigenstates of the Hamiltonian H_s in Eq. 1 are close to uncoupled donor and acceptor vibronic states represented in Fig. 1B, namely, $|D\rangle|n_-\rangle$ and $|A\rangle|n_+\rangle$, respectively. In this case, the $V_x\sigma_x$ term can be treated as a perturbation to the Hamiltonian $H_0 = H_s - V_x\sigma_x$. As a result, the transfer undergoes resonant transitions between the uncoupled donor and acceptor vibronic states, following the FGR (*30, 33, 44*)

$$k_T = 2\pi |V_x|^2 \sum_{n_-,n_+} p_{n_-}\,\mathrm{FC}_{n_-,n_+}\,\delta\!\left(E_{D,n_-} - E_{A,n_+}\right) \qquad (4)$$

where p_{n_-} is the initial phonon populations in the donor state, and $\mathrm{FC}_{n_-,n_+} = |\langle n_-|n_+\rangle|^2$ is the Franck-Condon factor, namely, the overlap between the two displaced Fock wave functions. A larger displacement g/ω along the reaction coordinate leads to more vibrational states with a non-negligible overlap, therefore increasing the number of observable transfer resonances.

In this regime, the effect of the bath can be taken into account by replacing the delta functions in Eq. 4 with normalized Lorentzian distributions with full width at half maximum γ, namely, $\delta\!\left(E_{D,n_-} - E_{A,n_+}\right) \rightarrow (\gamma/2\pi)/\left[\left(E_{D,n_-} - E_{A,n_+}\right)^2 + \left(\gamma^2/4\right)\right]$.

In Fig. 3A, we show the transfer rates extracted from the dynamics of the donor population $P_D(t)$, shown in Fig. 3B (experimental data) and Fig. 3C (theory) as density plots as a function of ΔE
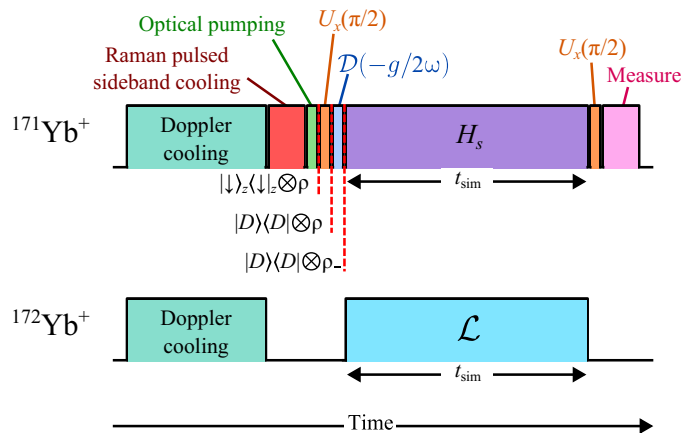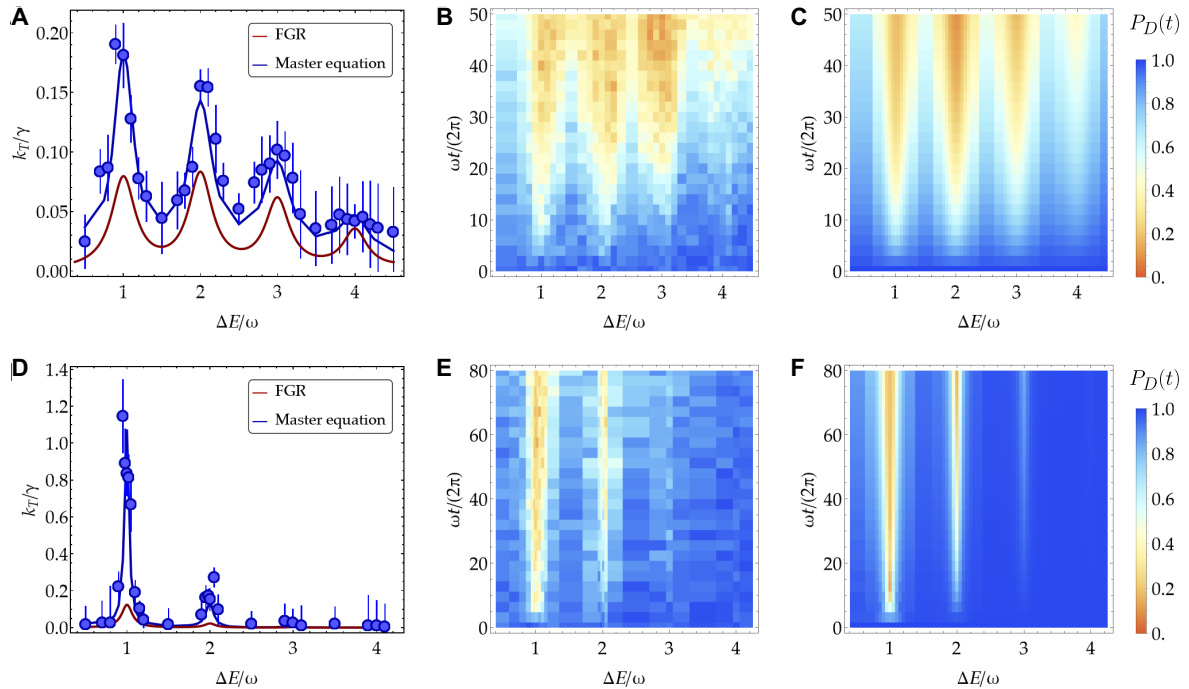

Fig. 2. Experimental protocol. After Doppler cooling, Raman sideband cooling, and optical pumping, the initial vibronic state $|D\rangle\langle D| \otimes \rho_-$ is prepared by a $\pi/2$ pulse along the x axis and by displacing the motional state via a spin-dependent force. Before the final measurement, another $\pi/2$ pulse along the x axis rotates the final spin state back into the qubit basis.

Fig. 3. Nonadiabatic transfer regime. (**A**) Transfer rate k_T in units of the relaxation rate γ as a function of the donor-acceptor energy gap ΔE for $(V_x, g, \gamma) = (0.056, 1.4, 0.06)\omega$. The blue points result from an exponential fit of the measured $P_D(t)$ dynamics, with the error bars being the standard errors of the fit. The dark blue solid curve is obtained from the fit of the dynamics predicted by Eq. 2. The FGR prediction (dark red solid line) is calculated using Eq. 4. (**B** and **C**) Experimental (B) and numerical (C) density plots of the time-resolved dynamics of $P_D(t)$ as a function of both ΔE and the number of vibrational oscillations $\omega t/2\pi$. The detuning from the tilt mode is set to $\delta/(2\pi) = -5$ kHz, and the numerical results include a motional dephasing of $\gamma_m = 0.001\omega$. (**D**) Transfer rate k_T in units of the relaxation rate γ as a function of the donor-acceptor energy gap ΔE for $(V_x, g, \gamma) = (0.046, 0.521, 0.025)\omega$. (**E** and **F**) Experimental (E) and numerical (F) density plots of the time-resolved dynamics of $P_D(t)$ as a function of both ΔE and the number of vibrational oscillations $\omega t/2\pi$, with $\delta/(2\pi) = -10$ kHz. The numerical results include a motional dephasing $\gamma_m = 0.0005\omega$ (see section S3).

and the number of vibrational oscillations $\omega t/2\pi$. The transfer rates extracted from an exponential decay fit of $P_D(t)$ agree with the numerical predictions from the Lindblad master equation in Eq. 2, exhibiting distinct peaks at $\Delta E = \ell\omega$. In Fig. 3 (A to C), the chosen parameters place the system in the nonadiabatic regime ($V_x = 0.056\omega$ and $\lambda/4 = 0.49\omega$), which is confirmed by the qualitative agreement between the FGR prediction (dark red solid line), the experimental results, and the exact theory. Here, because $g = 1.4\omega$, we can observe transfer resonances involving vibrational states up to $n = 4$ within our experimental resolution (see section S3).

In Fig. 3 (D to F), we decrease the spin-motion coupling to $g = 0.521\omega$ and the motional relaxation rate to $\gamma = 0.025\omega$ while keeping the values of the other parameters approximately the same as in Fig. 3 (A to C). In this case, by lowering the spin-motion coupling strength, the Franck-Condon coefficients FC_{n_-, n_+} are greater for smaller n compared to Fig. 3 (A to C). Therefore, fewer vibrational excitations are involved in the transfer through the effective vibronic coupling strength $V_x\sqrt{FC_{n_-, n_+}}$, resulting in the reduction in the number of observed resonances compared to Fig. 3 (A to C). In addition, the data in Fig. 3 (D to F) show that the FGR predictions in Eq. 4 further underestimate both the experimental and numerical results as the system is approaching the nonperturbative regime. Lastly, the decrease in the motional relaxation rate makes the width of the resonances sharper across the spectrum, confirming its connection with the broadening of the vibrational modes.

Strongly adiabatic regime

When the electronic coupling V_x is comparable to the activation barrier $\lambda/4$ and larger than the relaxation rate γ, the dynamics cannot be simply described in terms of weakly coupled wave function localized on the donor and acceptor site. In this regime, the population evolution features an initial coherent oscillation between the donor and acceptor states before the eventual equilibration in the acceptor state, as shown in Fig. 4 (B and C). Here, the density plots of the experimental and theoretical $P_D(t)$ are plotted as a function of ΔE, showing good agreement. In this regime, the evolution cannot be fitted with an exponential function as in the nonadiabatic case. Therefore, to extract the effective transfer rate, we use the inverse lifetime of the donor population as proposed in refs. (*33*, *44*)

$$k_T^{-1} = \frac{\int t P_D(t) dt}{\int P_D(t) dt} \tag{5}$$

In Fig. 4A, the transfer rates are extracted using Eq. 5 by interpolating and integrating both the experimental data and the numerical results (see Materials and Methods). We show the transfer rates extracted from the data for two sets of parameters that have nearly equal spin-phonon coupling g and electronic coupling V_x but different relaxation rates γ. We report the results in units of γ, showing that the transfer rate is proportional to the relaxation rate ($k_T \propto \gamma$). In this regime, γ becomes the limiting factor for the rate at which the donor state population irreversibly transfers into the acceptor state.
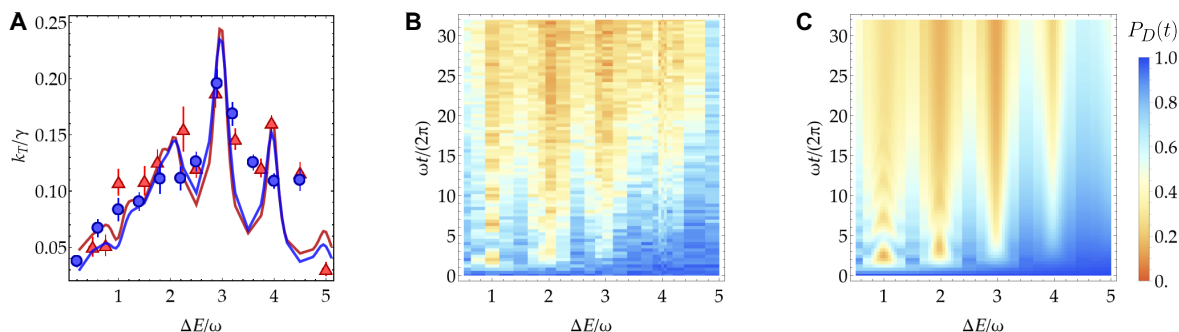
Fig. 4. Adiabatic transfer regime. (**A**) Transfer rate k_T measured with $(V_x, g, \gamma) = (0.18, 0.95, 0.020)\omega$ (red triangles) and $(V_x, g, \gamma) = (0.21, 1.08, 0.038)\omega$ (blue circles). The solid curves are the transfer rates calculated from Eq. 2 using the definition in Eq. 5 and including spin decoherence ($\gamma_z = 0.0025\omega$) and motional dephasing ($\gamma_m = 0.0013\omega$). The transfer rates overlap when scaled in units of the relaxation rate γ. The error bars are calculated using bootstrapping (see Materials and Methods). (**B**) Experimental donor population evolution $P_D(t)$ versus energy gap ΔE and the number of vibrational oscillations $\omega t/2\pi$ with the same parameters as the red triangles in (A). Here, the detuning from the tilt mode is set to $\delta/2\pi = -4$ kHz. (**C**) Corresponding numerical results with the same parameters as (B).

This result can be explained intuitively by considering a simplified two-vibronic-state model (33) consisting of the initial donor state $|D\rangle|0_-\rangle$ and a single acceptor vibronic state $|A\rangle|\nu_+\rangle$ with the coupling strength $V_x\sqrt{\mathrm{FC}_{0_-,\nu_+}}$ and a decay rate $\nu\gamma$, where $\nu = \Delta E/\omega$. In this simplified case, the transfer rate in Eq. 5 can be evaluated analytically as

$$k_T^{0,\nu} = \nu\gamma \frac{1 + \left(\dfrac{\nu\gamma}{V_x\sqrt{\mathrm{FC}_{0_-,\nu_+}}}\right)^2}{1 + \dfrac{1}{2}\left(\dfrac{\nu\gamma}{V_x\sqrt{\mathrm{FC}_{0_-,\nu_+}}}\right)^4} \qquad (6)$$

When $V_x\sqrt{\mathrm{FC}_{0_-,\nu_+}} \gg \gamma$, $k_T^{0,\nu} \approx \nu\gamma$. Although this approximation rightly predicts the proportionality between k_T and γ in the strongly adiabatic regime, it fails to accurately predict the transfer rates when more than one vibronic acceptor state is involved.

A few comments are in order: (i) For $\Delta E < 2\omega$, the transfer rate k_T does not exhibit distinct resonances as opposed to the transfer rate in the nonadiabatic regime. (ii) For $\Delta E > 2\omega$, the characteristic peaked structure of the nonadiabatic regime is recovered, which can be explained by the localization of the initial state in the upper hybridized surface, as suggested by ref. (33). (iii) For $\Delta E > 3\omega$, the envelope of the transfer rate shows a decrease as a function of ΔE. This is sometimes called the "inverted regime" of ET, where, at both high and low temperatures, the reaction counterintuitively becomes slower despite the transfer becoming more exothermic. This can be explained by the decreasing Franck-Condon factor FC_{n_-,n_+} as a function of ΔE and can also be observed in the nonadiabatic regime (see Fig. 3).

Optimal transfer

When ΔE is set on a resonance, sweeping V_x/γ allows one to pinpoint an optimal transfer regime (44). In Fig. 5, we report the transfer rate measured as a function of V_x/γ, setting $\Delta E = 2\omega$. The data exhibit a distinct optimal transfer rate at $V_x/\gamma \sim 3.3$, in good agreement with the numerical predictions based on Eq. 2. It is worth noting that, for small V_x/γ, the transfer rate varies quadratically as predicted by Eq. 4. Beyond the optimum, the transfer rate is less sensitive to V_x/γ. This robustness has been suggested to be important for fast transfer in photosynthetic complexes (44, 45). In particular, the presence of an

optimal relaxation rate underscores the crucial role of dephasing in transport phenomena that was previously pointed out in solid-state (46) and atomic systems (25), as well as in biomolecules (47–50).

DISCUSSION

Our experiment demonstrates the remarkable flexibility of the trapped-ion platform to perform direct analog quantum simulations of models relevant to chemical physics, including an engineered environment. These simulations are performed through careful tuning of both the Hamiltonian of the trapped-ion system and its engineered reservoir by using seven simultaneous laser tones and two different atomic species. This toolbox allowed us to investigate relevant regimes of a paradigmatic ET model with tunable dissipation at low temperatures, where the interplay of quantum effects and interactions with the environment is crucial
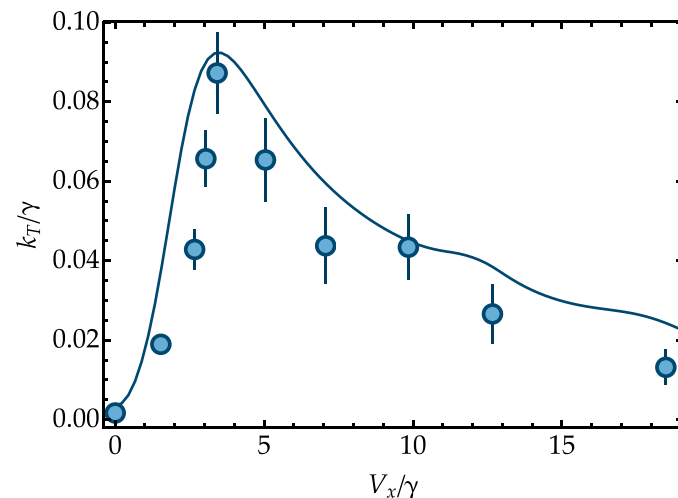

Fig. 5. Optimal transfer. Transfer rate k_T as a function of V_x/γ, with $(\Delta E, g, \gamma) = (2, 0.80, 0.11)\omega$ and detuning $\delta/2\pi = -4$ kHz. The numerical results (solid curve) include spin decoherence ($\gamma_z = 0.0013\omega$) and motional dephasing ($\gamma_m = 0.0013\omega$). The optimal transfer is located at $V_x/\gamma \sim 3.3$, in agreement with the theoretical prediction of Eq. 2. Error bars are calculated using bootstrapping (see Materials and Methods).

in determining the dynamics. The observed time-resolved dynamics of the donor-acceptor population and the measured transfer rate in both the nonadiabatic and adiabatic regimes agree with the numerics with independently calibrated parameters and identify an optimal transfer regime that has been suggested to be relevant for ET in photosynthetic complexes (*44*).

Our experiment opens up unexplored avenues for simulating condensed-phase chemical quantum dynamics. The trapped-ion simulator allows native encoding of the bosonic degrees of freedom and their tunable dissipation without the need for digitization, leading to linear scaling with both the number of electronic states and that of bosonic modes. In this context, existing classical numerical methods used to solve these models are more computationally expensive when the reorganization energy is of the same order or larger than the electronic coupling ($\lambda \gtrsim V_x$) (*5*, *17*). To access such a parameter range, it is necessary to experimentally realize nonperturbative spin-phonon couplings $g \gtrsim \omega$. Crucially, the approach used here based on sympathetic cooling gives rise to the dynamics of the corresponding spin-boson model with a Lorentzian spectral density at all orders in g under the assumptions used in this work ($\gamma \ll \omega, \gamma\beta \ll 1$) (*40*, *51*). Therefore, this approach will enable the realization of structured spectral density functions (*40*) and the simulation of colored baths and non-Markovian dynamics (*52*, *53*) by using multiple ions as coolants to control the individual cooling rates and the temperature of multiple bosonic modes.

To investigate the role of coherence and Frenkel-type exciton delocalization (*54*) in the energy transfer processes in biomolecules and photosynthetic complexes (*55*, *56*), a necessary extension is the encoding of multiple electronic excited states. This can be achieved using more than two atomic levels (a qudit) coupled to phonons (*34*) provided by the ion crystal. Alternatively, multiple electronic states (sites) can be physically mapped to qubit ions and individually addressed to tailor their energy landscape and their individual couplings to the phonon bath. At the same time, the site qubits will have to be connected via a long-range spin-hopping Hamiltonian that can be realized with Molmer-Sørensen Ising interactions (*57*). In addition, the trapped-ion platform naturally offers the possibility to include tunable anharmonic couplings among different bosonic modes (*58*) that can be used to study the effects of anharmonicity on energy transfer (*59*), a crucial but often overlooked feature of realistic molecular systems that hinders the applicability of existing numerical methods.

The native long-range character of the spin-spin interactions and the presence of collective bosonic modes with tunable dissipation and anharmonic couplings will allow the simulation of out-of-equilibrium chemical dynamics that are challenging to address with classical methods. Our experiment is therefore a stepping-stone toward the use of quantum devices to provide insights into open questions in chemical and biological physics and to shed light on the underlying principles of biochemical processes.

During the preparation of this manuscript, we became aware of a complementary work (*60*), which simulates the dephased spin-boson model using randomized unitary spin-dependent forces.

MATERIALS AND METHODS
Experimental system
The experimental system is based on a blade trap, where each blade features five segmented electrodes. We mounted the gold-coated fused silica blades on an alumina holder. Alumina is chosen for its high thermal conductivity and low outgassing rate. The blades are positioned in a 60°/30° angle configuration to enable high optical access along the vertical direction for high-resolution imaging [0.6 numerical aperture (NA)] and along the in-plane direction orthogonal to the trap axis (0.3 NA). This configuration also breaks rotational symmetry, which allows for well-defined trap principal axes. Each electrode is biased via a gold fuzz button, which is, in turn, connected to a Kapton-insulated wire via customized Macor holders. To shunt the radio frequency (rf) pickup voltages on the static dc blades, we use ultrahigh vacuum–compatible silver-filled epoxy to glue 800-pF capacitors to each static segment on one side and wire bond the other side to a ground strip present on the blades. We use a helical resonator with a resonant frequency of 27.9 MHz and a quality factor $Q = 198$ to drive the rf blades, achieving a radial center-of-mass trap frequency of 3.363 MHz at $V_{peak} = 420$ V. The heating rate on the radial center-of-mass mode is measured to be 0.4 quanta/ms, whereas the tilt mode features a lower heating rate ($\dot{n} \sim 0.03$ quanta/ms).

A 370-nm laser red detuned from the $^2S_{1/2} \rightarrow {}^2P_{1/2}$ transition passing through 3.704- and 14.748-GHz electro-optic modulators is used to produce Doppler cooling light for both isotopes ^{171}Yb$^+$ and ^{172}Yb$^+$. This beam is placed in-plane at 45° with respect to the ion chain for projection along all three trap principal axes. In addition, two axial 370-nm beams are used for detection and optical pumping of ^{171}Yb$^+$. They are also superimposed with two 935-nm repumper beams for both Yb$^+$ isotopes.

A pulsed 355-nm laser is used to resonantly address the ^{171}Yb$^+$ ground-state qubit via two-photon Raman processes. The same laser is used to generate the spin-phonon coupling. The counterpropagating Raman beams have elliptical shapes with vertical and horizontal waists $w_z = 5$ μm and $w_x = 150$ μm and are in lin⊥lin polarization configuration to maximize the coupling between the two hyperfine clock states.

A 435-nm diode laser locked to an ultralow expansion cavity is used to address the $^2S_{1/2} \rightarrow {}^2D_{3/2}$ transition (or $|g\rangle \rightarrow |o\rangle$) in ^{172}Yb$^+$ (*61*, *62*). The beam is aligned at 45° with respect to the magnetic field and horizontally polarized to maximize the coupling to the two $\Delta m_j = 0$ transitions ($m_j = \pm 1/2 \rightarrow m_{j'} = \pm 1/2$) separated by 8.23 MHz. The cooling is achieved by continuously driving the red sideband of $m_j = \pm 1/2 \rightarrow m_{j'} = \pm 1/2$ transitions while also using a 935-nm repumper laser that allows the transition between $|o\rangle$ and $^3D[3/2]_{1/2} \equiv |e\rangle$. Two tones on the 935-nm laser separated by 113 MHz address both ^{171}Yb$^+$ and ^{172}Yb$^+$. To avoid optical pumping into either of the $m_j = \pm 1/2$ ground states during continuous sideband cooling, we use two laser tones on the 435-nm laser to address both the $m_j = \pm 1/2 \rightarrow m_{j'} = \pm 1/2$ transitions simultaneously. The effective cooling rate is highly dependent on the power of the 935-nm laser, and it is the main turning knob to tune the cooling rate γ.

Experimental sequence
The experimental procedure is summarized in Fig. 2. Our setup consists of a ^{171}Yb$^+$ ion acting as the qubit and a ^{172}Yb$^+$ ion acting as the coolant. Initially, we use the standard Doppler cooling technique on both ions to prepare the temperature of the trapped dual-species chain near the Doppler limit. We then perform the Raman-resolved sideband cooling protocol on the radial center-of-mass and tilt

modes, followed by an optical pumping pulse, to prepare the system in $|\downarrow\rangle_z\langle\downarrow|_z \otimes \rho$, where $\rho = \sum_n e^{-n\omega/k_BT}|n\rangle\langle n|$ is the thermal phonon density matrix of the tilt mode and $k_BT = \omega/\log(1+1/\overline{n}_0)$ is the associated temperature. The initial tilt mode average phonon $\overline{n}_0$ is set to range between 0.1 and 0.3, which is similar to the bath temperature $\overline{n}$. To transform the system from the qubit basis σ_z to the σ_y basis, we apply a global rotation $U_x(\pi/2) = \exp(-i\sigma_x\pi/4)$. The state of the system becomes $|D\rangle\langle D| \otimes \rho$, where $|D\rangle \equiv |\uparrow\rangle_y$ here.

We then prepare the motional population from ρ to ρ_- with an optical dipole force from two Raman beatnotes, $\omega_r = \omega_{\text{hf}} - \mu$ and $\omega_b = \omega_{\text{hf}} + \mu$, which have the same Rabi coupling strength of $\Omega^{\text{displace}} = \Omega/2$, with $\eta\Omega = g$ and $\phi_r = \phi_b = \pi$. We point out that this is the same drive that generates the spin-phonon term in Eq. 1 but with half the Rabi coupling strength. This results in a spin-dependent displacement of the motional state

$$H_{\text{displace}}^{\text{eff}} = \frac{\eta\Omega^{\text{displace}}}{2}\sigma_y\left(ae^{i\delta t} + a^\dagger e^{-i\delta t}\right) \qquad (7)$$

where $\delta \equiv \mu - \omega_{\text{tilt}}$. Under this operation, the system evolves as $U(t) = \mathcal{D}[\alpha(t)]|\uparrow\rangle_y\langle\uparrow|_y + \mathcal{D}[-\alpha(t)]|\downarrow\rangle_y\langle\downarrow|_y \equiv \mathcal{D}[\alpha(t)]|D\rangle\langle D| + \mathcal{D}[-\alpha(t)]|A\rangle\langle A|$, where $\mathcal{D}$ is the displacement operator in position-momentum phase space and $\alpha(t) = \alpha_0(1 - e^{-i\delta t})$ with $\alpha_0 = \eta\Omega^{\text{displace}}/2\delta = g/4\delta$ (57). Hence, the applied pulse duration is $t_{\text{displace}} = \pi/\delta$ to get the displacement of $\alpha(t_{\text{displace}}) = g/2\delta = -g/2\omega$ onto ρ.

With the system being in the desired initial state $|D\rangle\langle D| \otimes \rho_-$, we address the $^{171}\text{Yb}^+$ with the four Raman beatnotes to generate an effective Hamiltonian that maps to the ET unitary model in Eq. 1 (see section S1). Simultaneously, we apply the continuous resolved sideband cooling protocol on the $^{172}\text{Yb}^+$'s narrow linewidth optical transition to sympathetically cool the tilt mode of the system at the rate γ and effectively realize an engineered phonon dissipation. By varying the simulation time t_{sim}, we can measure the time-dependent evolution of the system. Before the measurement, we rotate the system back to the qubit basis with another global rotation $U_x(\pi/2)$.

To measure the average spin excitation, we use spin-dependent fluorescence, where only the spin in state $|\uparrow\rangle_z$, now representing $|D\rangle$ after the $\pi/2$ global rotation, scatters photons. We use an objective lens with an NA of 0.6 to collect the scattered photons into the photomultiplier tube. The average state discrimination fidelity between $|D\rangle$ and $|A\rangle$ is 99.5%.

Alternatively, we can measure the average phonon excitation $\langle a^\dagger a\rangle$ by performing an optical pumping pulse to reset the spin state of the system to $|\downarrow\rangle_z$ followed by a resonant Raman blue sideband (BSB) transition drive, $H^{\text{BSB}} = i(\eta\Omega/2)(a\sigma^- - a^\dagger\sigma^+)$, before the average spin excitation measurement. The phonon-number distribution that represents the diagonal elements of the final phonon density matrix of the system, ρ_m, can be extracted by fitting the spin evolution under the resonant Raman BSB transition drive with

$$P_{|\uparrow\rangle_z}(t) = \frac{1}{2}\sum_n p(n)\left[1 - e^{-\alpha_m t}\cos\left(\sqrt{n+1}\eta\Omega t\right)\right] \qquad (8)$$

where $p(n)$ denotes the phonon-number state population, α_m is a parameter to capture the decoherence rate of the spin-phonon evolution, and t is the drive time (35). Hence, we can compute $\langle a^\dagger a\rangle = \text{Tr}(\rho_m a^\dagger a)$.

Transfer rate data analysis

In the nonadiabatic regime, the transfer dynamics can be well described by an exponential decay (see figs. S3, A and B). Because of the finite bath temperature $\overline{n} \sim 0.1$ to 0.3, the spin population transfer is not complete from $|D\rangle$ to $|A\rangle$. Therefore, the transfer rates are extracted from an exponential function with the rates and final populations as the fitting parameters. The uncertainties of the rates are the corresponding standard errors of the fits.

On the other hand, the spin evolutions in the adiabatic regime feature complex oscillatory decays that a simple analytical model cannot describe (see figs. S3, C and D). For this reason, we use the inverse lifetime of the donor population in Eq. 5 to determine the transfer rates (33, 44). This definition considers $t \to \infty$; therefore, there is a correction we need to consider when we use this formula for a finite experimental time. In the case of no electronic coupling, $V_x = 0$, the donor population does not evolve, $P_D(t) = 1$, because it is in an eigenstate of the system. However, Eq. 5 still evaluates a nonzero transfer rate between $t = 0$ and $t = t_{\text{sim}}$ as $k_0 = \frac{2}{t_{\text{sim}}}$. This contribution to the transfer rate only goes to zero if one evaluates Eq. 5 for $t \to \infty$. Because P_D reaches the steady state within our experimental resolution in a finite time t_{sim} ranging from 4 to 10 ms, we calculate the transfer rates by subtracting k_0 as

$$k_T = \frac{\int_0^{t_{\text{sim}}} P_D(t)dt}{\int_0^{t_{\text{sim}}} tP_D(t)dt} - k_0 \qquad (9)$$

To numerically evaluate the integrals, we interpolate the evolution $P_D(t)$ data. We also use Eq. 9 to estimate the numerical transfer rates.

To estimate the errors of the transfer rate, we follow a resampling procedure. We consider the experimental error of each time step of the $P_D(t)$ measurements as the SD of a normal distribution centered at the mean measured value. We then randomly sample the distributions at each time step, and we estimate the error of the transfer rate by taking the SD of the rates obtained from the resampled datasets by using Eq. 9. The process is repeated for all adiabatic transfer dynamics.

Supplementary Materials

This PDF file includes:
Supplementary sections S1 to S6
Figs. S1 to S4
References

REFERENCES AND NOTES

1. A. J. Daley, I. Bloch, C. Kokail, S. Flannigan, N. Pearson, M. Troyer, P. Zoller, Practical quantum advantage in quantum simulation. *Nature* **607**, 667–676 (2022).
2. M. Reiher, N. Wiebe, K. M. Svore, D. Wecker, M. Troyer, Elucidating reaction mechanisms on quantum computers. *Proc. Natl. Acad. Sci. U.S.A.* **114**, 7555–7560 (2017).
3. N. Maskara, S. Ostermann, J. Shee, M. Kalinowski, A. M. Gomez, R. A. Bravo, D. S. Wang, A. I. Krylov, N. Y. Yao, M. Head-Gordon, M. D. Lukin, S. F. Yelin, Programmable simulations of molecules and materials with reconfigurable quantum processors. arXiv:2312.02265 [quant-ph] (2023).
4. S. Mostame, J. Huh, C. Kreisbeck, A. J. Kerman, T. Fujita, A. Eisfeld, A. Aspuru-Guzik, Emulation of complex open quantum systems using superconducting qubits. *Quantum Inf. Process.* **16**, 44 (2017).
5. M. Kang, H. Nuomin, S. N. Chowdhury, J. L. Yuly, K. Sun, J. Whitlow, J. Valdiviezo, Z. Zhang, P. Zhang, D. N. Beratan, K. R. Brown, Seeking a quantum advantage with trapped-ion

quantum simulations of condensed-phase chemical dynamics. *Nat. Rev. Chem.* **8**, 340–358 (2024).

6. H. Frauenfelder, P. G. Wolynes, Rate theories and puzzles of hemeprotein kinetics. *Science* **229**, 337–345 (1985).

7. R. Zhuravel, H. Huang, G. Polycarpou, S. Polydorides, P. Motamarri, L. Katrivas, D. Rotem, J. Sperling, L. A. Zotti, A. B. Kotlyar, J. C. Cuevas, V. Gavini, S. S. Skourtis, D. Porath, Backbone charge transport in double-stranded DNA. *Nat. Nanotechnol.* **15**, 836–840 (2020).

8. P. G. Wolynes, Imaginary time path integral Monte Carlo route to rate coefficients for nonadiabatic barrier crossing. *J. Chem. Phys.* **87**, 6559–6561 (1987).

9. C. Zheng, J. A. McCammon, P. G. Wolynes, Quantum simulation of nuclear rearrangement in electron transfer reactions. *Proc. Natl. Acad. Sci. U.S.A.* **86**, 6441–6444 (1989).

10. J. E. Lawrence, D. E. Manolopoulos, Path integral methods for reaction rates in complex systems. *Faraday Discuss.* **221**, 9–29 (2020).

11. E. R. Bittner, P. J. Rossky, Quantum decoherence in mixed quantum-classical systems: Nonadiabatic processes. *J. Chem. Phys.* **103**, 8130–8143 (1995).

12. G. D. Scholes, G. R. Fleming, L. X. Chen, A. Aspuru-Guzik, A. Buchleitner, D. F. Coker, G. S. Engel, R. van Grondelle, A. Ishizaki, D. M. Jonas, J. S. Lundeen, J. K. McCusker, S. Mukamel, J. P. Ogilvie, A. Olaya-Castro, M. A. Ratner, F. C. Spano, K. B. Whaley, X. Zhu, Using coherence to enhance function in chemical and biophysical systems. *Nature* **543**, 647–656 (2017).

13. L. Wang, M. A. Allodi, G. S. Engel, Quantum coherences reveal excited-state dynamics in biophysical systems. *Nat. Rev. Chem.* **3**, 477–490 (2019).

14. Y. Tanimura, Numerically "exact" approach to open quantum dynamics: The hierarchical equations of motion (HEOM). *J. Chem. Phys.* **153**, 020901 (2020).

15. A. Strathearn, P. Kirton, D. Kilda, J. Keeling, B. W. Lovett, Efficient non-Markovian quantum dynamics using time-evolving matrix product operators. *Nat. Commun.* **9**, 3322 (2018).

16. D. Tamascelli, A. Smirne, J. Lim, S. F. Huelga, M. B. Plenio, Efficient simulation of finite-temperature open quantum systems. *Phys. Rev. Lett.* **123**, 090402 (2019).

17. A. D. Somoza, O. Marty, J. Lim, S. F. Huelga, M. B. Plenio, Dissipation-assisted matrix product factorization. *Phys. Rev. Lett.* **123**, 100502 (2019).

18. N. Makri, Modular path integral methodology for real-time quantum dynamics. *J. Chem. Phys.* **149**, 214108 (2018).

19. S. Kundu, N. Makri, Real-time path integral simulation of exciton-vibration dynamics in light-harvesting bacteriochlorophyll aggregates. *J. Phys. Chem. Lett.* **11**, 8783–8789 (2020).

20. D. J. Gorman, B. Hemmerling, E. Megidish, S. A. Moeller, P. Schindler, M. Sarovar, H. Haeffner, Engineering vibrationally assisted energy transfer in a trapped-ion quantum simulator. *Phys. Rev. X* **8**, 011038 (2018).

21. J. Whitlow, Z. Jia, Y. Wang, C. Fang, J. Kim, K. R. Brown, Quantum simulation of conical intersections using trapped ions. *Nat. Chem.* **15**, 1509–1514 (2023).

22. C. H. Valahu, V. C. Olaya-Agudelo, R. J. MacDonell, T. Navickas, A. D. Rao, M. J. Millican, J. B. Pérez-Sánchez, J. Yuen-Zhou, M. J. Biercuk, C. Hempel, T. R. Tan, I. Kassal, Direct observation of geometric-phase interference in dynamics around a conical intersection. *Nat. Chem.* **15**, 1503–1508 (2023).

23. C. S. Wang, N. E. Frattini, B. J. Chapman, S. Puri, S. M. Girvin, M. H. Devoret, R. J. Schoelkopf, Observation of wave-packet branching through an engineered conical intersection. *Phys. Rev. X* **13**, 011008 (2023).

24. A. Potočnik, A. Bargerbos, F. A. Y. N. Schröder, S. A. Khan, M. C. Collodo, S. Gasparinetti, Y. Salathé, C. Creatore, C. Eichler, H. E. Türeci, A. W. Chin, A. Wallraff, Studying light-harvesting models with superconducting circuits. *Nat. Commun.* **9**, 904 (2018).

25. C. Maier, T. Brydges, P. Jurcevic, N. Trautmann, C. Hempel, B. P. Lanyon, P. Hauke, R. Blatt, C. F. Roos, Environment-assisted quantum transport in a 10-qubit network. *Phys. Rev. Lett.* **122**, 050501 (2019).

26. K. Sun, C. Fang, M. Kang, Z. Zhang, P. Zhang, D. N. Beratan, K. R. Brown, J. Kim, Quantum simulation of polarized light-induced electron transfer with a trapped-ion qutrit system. *J. Phys. Chem. Lett.* **14**, 6071–6077 (2023).

27. C. Sparrow, E. Martín-López, N. Maraviglia, A. Neville, C. Harrold, J. Carolan, Y. N. Joglekar, T. Hashimoto, N. Matsuda, J. L. O'Brien, D. P. Tew, A. Laing, Simulating the vibrational quantum dynamics of molecules using photonics. *Nature* **557**, 660–667 (2018).

28. H. Rohde, S. T. Gulde, C. F. Roos, P. A. Barton, D. Leibfried, J. Eschner, F. Schmidt-Kaler, R. Blatt, Sympathetic ground-state cooling and coherent manipulation with two-ion crystals. *J. Opt. B. Quantum Semiclassical Opt.* **3**, S34–S41 (2001).

29. B. B. Blinov, I. Deslauriers, P. Lee, M. J. Madsen, R. Miller, C. Monroe, Sympathetic cooling of trapped Cd^+ isotopes. *Phys. Rev. A* **65**, 040304 (2002).

30. A. J. Leggett, S. Chakravarty, A. T. Dorsey, M. P. A. Fisher, A. Garg, W. Zwerger, Dynamics of the dissipative two-state system. *Rev. Mod. Phys.* **59**, 1 (1987).

31. A. Garg, J. N. Onuchic, V. Ambegaokar, Effect of friction on electron transfer in biomolecules. *J. Chem. Phys.* **83**, 4491–4503 (1985).

32. P. G. Wolynes, Dissipation, tunneling, and adiabaticity criteria for curve crossing problems in the condensed phase. *J. Chem. Phys.* **86**, 1957–1966 (1987).

33. F. Schlawin, M. Gessner, A. Buchleitner, T. Schätz, S. S. Skourtis, Continuously parametrized quantum simulation of molecular electron-transfer reactions. *PRX Quantum* **2**, 010314 (2021).

34. R. J. MacDonell, C. E. Dickerson, C. J. T. Birch, A. Kumar, C. L. Edmunds, M. J. Biercuk, C. Hempel, I. Kassal, Analog quantum simulation of chemical dynamics. *Chem. Sci.* **12**, 9794–9805 (2021).

35. D. Lv, S. An, Z. Liu, J. N. Zhang, J. S. Pedernales, L. Lamata, E. Solano, K. Kim, Quantum simulation of the quantum Rabi model in a trapped ion. *Phys. Rev. X* **8**, 021027 (2018).

36. R. Marcus, N. Sutin, Electron transfers in chemistry and biology. *Biochim. Biophys. Acta* **811**, 265–322 (1985).

37. T. D. Lee, F. E. Low, D. Pines, The motion of slow electrons in a polar crystal. *Phys. Rev.* **90**, 297–302 (1953).

38. G. Clos, D. Porras, U. Warring, T. Schaetz, Time-resolved observation of thermalization in an isolated quantum system. *Phys. Rev. Lett.* **117**, 170401 (2016).

39. G. X. Wang, Y. K. Wu, R. Yao, W. Q. Lian, Z. J. Cheng, Y. L. Xu, C. Zhang, Y. Jiang, Y. Z. Xu, B. X. Qi, P. Y. Hou, Z. C. Zhou, L. He, L. M. Duan, Simulating the spin-boson model with a controllable reservoir in an ion trap. *Phys. Rev. A* **109**, 062402 (2024).

40. A. Lemmer, C. Cormick, D. Tamascelli, T. Schaetz, S. F. Huelga, M. B. Plenio, A trapped-ion simulator for spin-boson models with structured environments. *New J. Phys.* **20**, 073002 (2018).

41. C. Schneider, D. Porras, T. Schaetz, Experimental quantum simulations of many-body physics with trapped ions. *Rep. Prog. Phys.* **75**, 024401 (2012).

42. M. Cetina, L. N. Egan, C. Noel, M. L. Goldman, D. Biswas, A. R. Risinger, D. Zhu, C. Monroe, Control of transverse motion for quantum gates on individually addressed atomic qubits. *PRX Quantum* **3**, 010334 (2022).

43. K. D. Demadis, C. M. Hartshorn, T. J. Meyer, The localized-to-delocalized transition in mixed-valence chemistry. *Chem. Rev.* **101**, 2655–2686 (2001).

44. S. S. Skourtis, A. J. R. Da Silva, W. Bialek, J. N. Onuchic, New look at the primary charge separation in bacterial photosynthesis. *J. Phys. Chem.* **96**, 8034–8041 (1992).

45. J. N. Onuchic, P. G. Wolynes, Classical and quantum pictures of reaction dynamics in condensed matter: Resonances, dephasing, and all that. *J. Phys. Chem.* **92**, 6495–6503 (1988).

46. D. E. Logan, P. G. Wolynes, Dephasing and Anderson localization in topologically disordered systems. *Phys. Rev. B* **36**, 4135–4147 (1987).

47. M. B. Plenio, S. F. Huelga, Dephasing-assisted transport: Quantum networks and biomolecules. *New J. Phys.* **10**, 113019 (2008).

48. P. G. Wolynes, Some quantum weirdness in physiology. *Proc. Natl. Acad. Sci. U.S.A.* **106**, 17247–17248 (2009).

49. P. Rebentrost, M. Mohseni, I. Kassal, S. Lloyd, A. Aspuru-Guzik, Environment-assisted quantum transport. *New J. Phys.* **11**, 033003 (2009).

50. A. W. Chin, A. Datta, F. Caruso, S. F. Huelga, M. B. Plenio, Noise-assisted energy transfer in quantum networks and light-harvesting complexes. *New J. Phys.* **12**, 065002 (2010).

51. D. Tamascelli, A. Smirne, S. F. Huelga, M. B. Plenio, Nonperturbative treatment of non-Markovian dynamics of open quantum systems. *Phys. Rev. Lett.* **120**, 030402 (2018).

52. I. de Vega, D. Alonso, Dynamics of non-Markovian open quantum systems. *Rev. Mod. Phys.* **89**, 015001 (2017).

53. P. M. Harrington, E. J. Mueller, K. W. Murch, Engineered dissipation for quantum information science. *Nat. Rev. Phys.* **4**, 660–671 (2022).

54. S. J. Jang, B. Mennucci, Delocalized excitons in natural light-harvesting complexes. *Rev. Mod. Phys.* **90**, 035003 (2018).

55. A. Ishizaki, G. R. Fleming, Theoretical examination of quantum coherence in a photosynthetic system at physiological temperature. *Proc. Natl. Acad. Sci. U.S.A.* **106**, 17255–17260 (2009).

56. A. Mattioni, F. Caycedo-Soler, S. F. Huelga, M. B. Plenio, Design principles for long-range energy transfer at room temperature. *Phys. Rev. X* **11**, 041003 (2021).

57. C. Monroe, W. C. Campbell, L. M. Duan, Z. X. Gong, A. V. Gorshkov, P. W. Hess, R. Islam, K. Kim, N. M. Linke, G. Pagano, P. Richerme, C. Senko, N. Y. Yao, Programmable quantum simulations of spin systems with trapped ions. *Rev. Mod. Phys.* **93**, 025001 (2021).

58. S. Ding, G. Maslennikov, R. Hablützel, D. Matsukevich, Cross-Kerr nonlinearity for phonon counting. *Phys. Rev. Lett.* **119**, 193602 (2017).

59. C. Zhang, M. Gruebele, D. E. Logan, P. G. Wolynes, Surface crossing and energy flow in many-dimensional quantum systems. *Proc. Natl. Acad. Sci. U.S.A.* **120**, e2221690120 (2023).

60. K. Sun, M. Kang, H. Nuomin, G. Schwartz, D. N. Beratan, K. R. Brown, J. Kim, Quantum simulation of spin-boson models with structured bath. arXiv:2405.14624 [quant-ph] (2024).

61. C. Tamm, N. Huntemann, B. Lipphardt, V. Gerginov, N. Nemitz, M. Kazda, S. Weyers, E. Peik, Cs-based optical frequency measurement using cross-linked optical and microwave oscillators. *Phys. Rev. A* **89**, 023820 (2014).

62. D. T. C. Allcock, W. C. Campbell, J. Chiaverini, I. L. Chuang, E. R. Hudson, I. D. Moore, A. Ransford, C. Roman, J. M. Sage, D. J. Wineland, *omg* blueprint for trapped ion quantum computing with metastable states. *Appl. Phys. Lett.* **119**, 214002 (2021).

63. J. Johansson, P. Nation, F. Nori, QuTiP 2: A Python framework for the dynamics of open quantum systems. *Comput. Phys. Commun.* **184**, 1234–1240 (2013).

64. C. Flühmann, T. L. Nguyen, M. Marinelli, V. Negnevitsky, K. Mehta, J. P. Home, Encoding a qubit in a trapped-ion mechanical oscillator. *Nature* **566**, 513–517 (2019).

65. S. F. Huelga, A. Rivas, M. B. Plenio, Non-Markovianity-assisted steady state entanglement. *Phys. Rev. Lett.* **108**, 160402 (2012).

66. H.-P. Breuer, F. Petruccione, *The Theory of Open Quantum Systems* (Oxford Univ. Press, 2007).

67. H. J. Carmichael, Statistical Methods in Quantum Optics 1: Master Equations and Fokker-Planck Equations (Springer Science & Business Media, 2013).

68. T. Brandes, "Quantum dissipation" in *Lectures on Background to Quantum Information* (TU Berlin, 2004).

69. M. Mohseni, Y. Omar, G. S. Engel, M. B. Plenio, *Quantum Effects in Biology* (Cambridge Univ. Press, 2014).

70. M. A. Nielsen, I. L. Chuang, *Quantum Computation and Quantum Information* (Cambridge Univ. Press, 2001), vol. 2.